



Carbon nitride coupled with CdS-TiO₂ nanodots as 2D/0D ternary composite with enhanced photocatalytic H₂ evolution: A novel efficient three-level electron transfer process

Zhifeng Jiang ^{a,b,*}, Kun Qian ^a, Chengzhang Zhu ^a, Hongli Sun ^b, Weiming Wan ^c, Jimin Xie ^a, Huaming Li ^a, Po Keung Wong ^{b,**}, Shouqi Yuan ^{a,***}

^a Institute for Energy Research, School of Chemistry and Chemical Engineering, Jiangsu University, Zhenjiang, Jiangsu 212013, PR China

^b School of Life Sciences, The Chinese University of Hong Kong, Shatin, NT, PR China

^c Department of Chemical Engineering, Columbia University, New York, NY 10027, United States

ARTICLE INFO

Article history:

Received 11 January 2017

Received in revised form 11 March 2017

Accepted 27 March 2017

Available online 29 March 2017

Keywords:

TiO₂-CdS nanodots

Carbon nitride

Photocatalysis

H₂-generation

ABSTRACT

Photocatalytic H₂ evolution from water splitting requires an efficient photocatalyst with excellent charge separation ability and broad visible-light adsorption region. 0D CdS-TiO₂ nanodots (NDs) were successfully decorated on the 2D g-C₃N₄ sheets via an epitaxial growth process. The as-synthesized ternary composite of CdS-TiO₂@g-C₃N₄ exhibits enhanced visible-light-driven photocatalytic H₂ evolution activity, as compared to the binary composites and their single components, which is about 6.7 and 11.2 times higher than those of single CdS and g-C₃N₄, respectively. Moreover, the as-obtained ternary composite has an external quantum efficiency (EQE) of 11.9% at 420 nm, implying the high utilization efficiency of photo-induced charges. In addition, the superior photostability can be achieved by this coupling method. The enhanced photocatalytic activity was attributed to the efficient charge separation originated from the three-level electron transfer system, the matched energy level positions, the abundant adsorption sites and active sites (0D/2D structure) and the synergistic effect among CdS, TiO₂ and g-C₃N₄. The work present here demonstrated that the construction of this three-level electron transfer system is an effective strategy to design more efficient ternary materials toward solar energy conversion (like H₂ production and CO₂ reduction).

© 2017 Elsevier B.V. All rights reserved.

1. Introduction

The depletion of energy resources and environment problems are two of the most urgent issues facing modern society. Heterogeneous photocatalysis has been emerged as a green and efficient technology to solve these issues due to the economical usage of catalysts and solar energy. Among these photocatalytic reaction, photocatalytic H₂ evolution from water splitting over semiconductors by solar irradiation has attracted extensively research attention due to its potential application in hydrogen economy [1,2]. Among various semiconductors, anatase TiO₂ is regarded as one of the most promising photocatalysts, owing to its excellent

stability, cheapness and non-toxicity. However, it is mainly photosensitive in the ultraviolet wavelength range, which makes up only 3–5% of the solar spectrum. Moreover, the high recombination rate of photo-generated carriers also leads to its low overall efficiency [3,4]. To this end, considerable researches have been conducted to find methods to solve the above-mentioned issues. Coupling TiO₂ with a narrow band-gap semiconductor to form a heterostructure is proved to be an effective strategy to extend the visible light response of TiO₂-based composite materials and efficiently improve the separation of charge carriers, consequently improving the photocatalytic performance. The built-in electric field formed between two semiconductors makes the photo-induced charge carriers transfer to opposite directions, thus prolonging the lifetime of the electrons and holes [5–7].

Cadmium sulfide (CdS) is known as an intriguing n-type photocatalyst, and has been proved to be an excellent sensitizer to extend the light adsorption range of oxide semiconductor with wide bandgap due to its narrow bandgap of 2.4 eV [8–11]. Moreover, since the conduction band position of CdS (~ -0.52 eV vs.

* Corresponding author at: Institute for Energy Research, School of Chemistry and Chemical Engineering, Jiangsu University, Zhenjiang, Jiangsu 212013, PR China.

** Corresponding author.

*** Corresponding author.

E-mail addresses: njjiangzf@sina.com (Z. Jiang), pkwong@cuhk.edu.hk (P.K. Wong), shouqiy@ujs.edu.cn (S. Yuan).

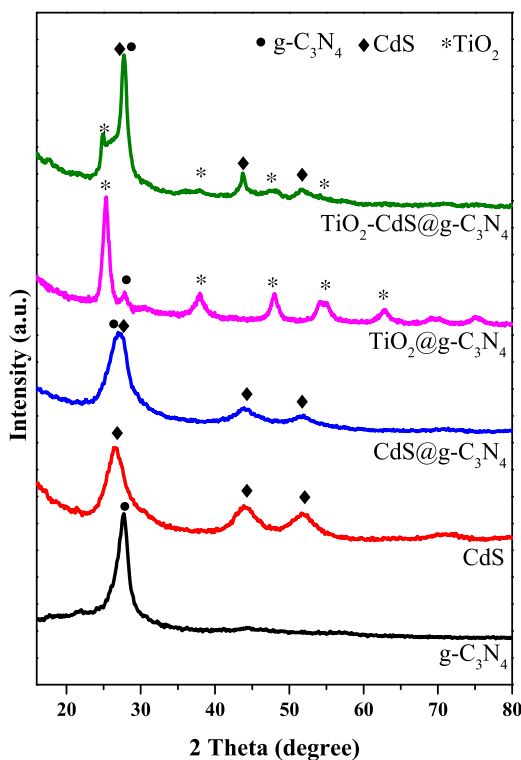


Fig. 1. Wide-angle XRD patterns of as-prepared $\text{g-C}_3\text{N}_4$, CdS, $\text{CdS}@\text{g-C}_3\text{N}_4$, $\text{TiO}_2@\text{g-C}_3\text{N}_4$ and $\text{TiO}_2\text{-CdS}@\text{g-C}_3\text{N}_4$.

NHE) is more negative than the standard reduction potential of H^+/H_2 , it is considered as a suitable photocatalyst for solar-driven hydrogen evolution. Nevertheless, some drawbacks still associated with such semiconductor material, such as the rapid charge recombination and the well-known photocorrosion induced by the photo-induced holes [12,13]. It is reported that constructing CdS with other semiconductors is an effective way to solve this problem [14–18]. For example, the coupling of CdS with appropriate TiO_2 contents has been proved to possess improved photocatalytic activities and good stability. Bian [19] and co-workers reported a CdS quantum dots-sensitized, (001) facets exposed TiO_2 mesocrystal with high activity and stability in visible photocatalysis for selective alcohol oxidations. Li [20] et al. developed a durable CdS-doped TiO_2 visible photocatalyst with high activity in photocatalytic degradation of 4-chlorophenol. Zhang [21] group prepared fullerene modified CdS/ TiO_2 composites using a sol-gel method that exhibits enhanced vis-photocatalytic activity towards the degradation of methylene blue. However, TiO_2/CdS hybrid photocatalyst with high H_2 -evolution activities are still very rare [22]. In addition, TiO_2/CdS nanocrystals with high surface energy tends to form agglomerates to minimize their surface area. Thus, it is desirable to obtain an effective strategy to increase the available active sites/surface area of the nanocrystal through incorporation a useful support. In this regard, a polymeric semiconductor with visible-light absorption, 2D graphite carbon nitride ($\text{g-C}_3\text{N}_4$) would be a favorable choice owing to its unique 2D sheet providing a large accessible surface platform and suitable band structure/location [23–25]. It can not only disperse nanocrystals onto itself without aggregation (improve active sites for photocatalytic reaction) but also improve light utilization as well as the separation efficiency of photo-generated electrons and holes. Li [26] and co-workers developed an in situ microwave-assisted synthesis approach to prepare $\text{N-TiO}_2/\text{g-C}_3\text{N}_4$ composites with porous structure and large surface areas using H_2TiO_3 as the reactant, and the composite showed enhanced visible-light photocatalytic properties towards

the degradation of rhodamine B (RhB) and methylene blue (MB). Huang [27] group reported a Ti^{3+} self-doped $\text{TiO}_2/\text{g-C}_3\text{N}_4$ heterojunctions by mixture of $\text{H}_2\text{Ti}_3\text{O}_7$ and melamine with high photocatalytic performance under LED light irradiation. Yu [28] et al. prepared $\text{CdS}/\text{g-C}_3\text{N}_4$ core/shell nanowires with H_2 production value of up to $4152 \mu\text{mol h}^{-1} \text{g}^{-1}$.

Herein, we present a facile strategy to plant 0D CdS- TiO_2 nanodots (NDs) on the 2D $\text{g-C}_3\text{N}_4$ sheets via an epitaxial growth process. To the best of our knowledge, it is the first time to report on the fabrication and application of this ternary composite for hydrogen evolution from water splitting. The as-prepared CdS- $\text{TiO}_2/\text{g-C}_3\text{N}_4$ composite shows enhanced H_2 production activity via photocatalytic water splitting and excellent photostability under visible light irradiation, which could be attributed to the fast and long-distance electron transport of the three-level electron transfer system, the broad visible-light harvesting ability of CdS NDs, the abundant adsorption sites and active sites (the large contact area provided by the unique 0D-2D structure) and the matched energy level positions. The possible photocatalytic mechanism for the water splitting of the ternary photocatalyst was also investigated. This work provided here can open up a simple yet effective wet chemical strategy toward the design and practical application of highly active visible-light photocatalysts via boosting photo-induced charge carriers separation and transfer efficiency.

2. Experimental section

2.1. Materials

Absolute ethanol ($\text{C}_2\text{H}_5\text{OH}$), tetrabutyl titanate (TBT), dimethyl sulphoxide (DMSO) and urea are of analytical grade and obtained from Sinopharm Chemical Reagent Co., LTD. Cadmium acetate ($\text{Cd}(\text{CH}_3\text{COO})_2 \cdot 2\text{H}_2\text{O}$) was bought from Aladdin Reagent Co., Ltd. All chemicals were of analytical grade and used as purchased without further purification. Deionized water was used for all experiments.

2.2. Preparation of $\text{g-C}_3\text{N}_4$ nanosheets

The $\text{g-C}_3\text{N}_4$ nanosheets were prepared by a thermal polymerization strategy [29,30]. Typically, 20 g of urea in a crucible with a cover were heated to 600°C at a heating rate of $5^\circ\text{C}/\text{min}$ in a tube furnace for 4 h in air. The resulted final light yellow powder was washed with distilled water and absolute ethanol to remove any residual alkaline species adsorbed on the sample surface, and then dried at 60°C for 24 h.

2.3. Preparation of $\text{TiO}_2\text{-CdS}@\text{g-C}_3\text{N}_4$ photocatalyst

The $\text{TiO}_2\text{-CdS}@\text{g-C}_3\text{N}_4$ composites were fabricated by a facile one-step hydrothermal approach. Firstly, 0.1 g of $\text{g-C}_3\text{N}_4$ was dispersed in DMSO (40 mL) under ultrasonic bath for 60 min. Then, $\text{Cd}(\text{CH}_3\text{COO})_2 \cdot 2\text{H}_2\text{O}$ (0.05 g), TBT (0.1 mL) and H_2O (0.1 mL) were added to the above injected into the above faint yellow suspension under a rate of 1.0 mL min^{-1} . Then the mixture was well dispersed by stirring for 30 min and then the result homogeneous suspension was transferred into a Teflon-lined autoclave with a capacity of 50 mL, followed by hydrothermal treatment at 180°C for 12 h. Finally, the as-prepared samples were centrifuged, washed with ethanol for 6 times and dried at a temperature of 60°C overnight to remove the absolute ethanol for the subsequent use and characterizations.

2.4. Characterization

The crystal structure and phase purity of the prepared samples were analysed by X-ray diffraction (XRD) using D8 Advance X-ray

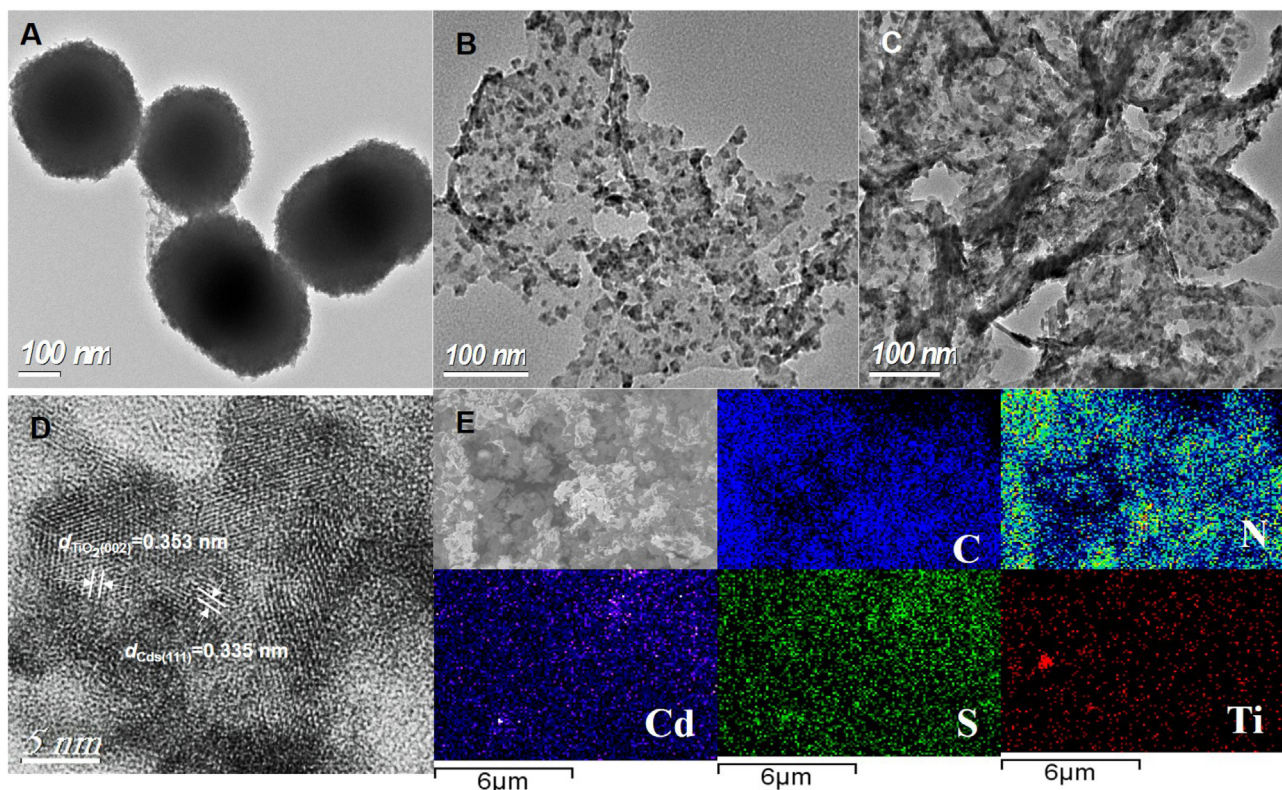


Fig. 2. TEM images of CdS (A), CdS@g-C₃N₄ (B) and TiO₂-CdS@g-C₃N₄ (C); HRTEM image (D) and EDS mapping (E) of TiO₂-CdS@g-C₃N₄.

diffractometer (Bruker axs company, Germany) equipped with Cu-K α radiation ($\lambda=1.5406 \text{ \AA}$), employing a scanning rate of $0.02^\circ \text{ s}^{-1}$ in the 2θ range from 20 to 80° . Scanning electron microscopy (SEM) was performed on a scanning electron microscope (Hitachi S-4800 II, Japan) operated at an acceleration voltage of 10 kV to characterize the morphologies and the compositions of the prepared samples. Furthermore, the morphology and particle size of the products were also examined by transmission electron microscopy (TEM) which was recorded on a JEOL-JEM-2010 (JEOL, Japan) operating at 200 kV . The optical properties of the samples were analyzed by UV-vis diffuse reflectance spectroscopy (DRS) using a UV-vis spectrophotometer. A Nicolet NEXUS470 FTIR spectrometer was applied to obtain Fourier transform infrared spectra. The resolution used for FTIR is 4 cm^{-1} . X-ray photoelectron spectroscopy (XPS) analysis was measured on an ESCALAB MK X-ray photo-electron spectrometer. The binding energies were calibrated by the aliphatic adventitious hydrocarbon C1 s peak at 284.8 eV . The excitation light employed in recording fluorescence spectra was 362 nm . The PL spectra of the samples were obtained by a QuantaMaster & TimeMaster Spectrofluorometer (QuantaMasterTM40, USA). Photocurrent measurements was performed on CHI 760B electrochemical analyzer (Chenhua Instruments Company, China).

2.5. Photoelectrochemical measurements

The electrochemical measurements were carried out in a three-electrode quartz cells (an electrochemical workstation, CHI760B). Pt wire was used as the counter electrode and saturated calomel electrodes (SCE) as the reference electrode. The working electrode was obtained according to the following process: 2 mg of catalyst and 0.01 g ethyl cellulose were added to ethanol solution, followed by being grinded into fine slurries. The above-prepared aqueous solution was spread on the pretreated ITO ($0.5 \text{ cm} \times 1 \text{ cm}$), and dried in air at room temperature to form photocatalysts modified

ITO. A 500 W Xe arc lamp was utilized as the light source in the photoelectrochemical measurements.

2.6. Photocatalytic water splitting for H₂ evolution

Hydrogen production experiments were carried out in an online photocatalytic hydrogen production system in a 100 mL Pyrex flask connected to a closed gas circulation and evacuation system. Four LEDs (3 W , 420 nm) (Shenzhen LAMPLIC Science Co. Ltd. China), used as light sources to trigger the photocatalytic reaction, were positioned 1 cm away from the reactor in four different directions. 50 mg of photocatalyst loaded with co-catalysts Pt nanoparticles (1 wt\% , using the in-situ photodeposition method) was dispersed by magnetic stirrer in 80 mL of aqueous solution containing 0.5 M Na₂S and 0.5 M Na₂SO₃. Prior to irradiation, the suspension was sonicated for 10 min and purged with nitrogen for 20 min to remove all air in solution and headspace and ensure the reactor was in an anaerobic condition. The illumination intensity at the catalyst surface is 120.0 mW . A 0.4 mL gas was intermittently sampled through the septum, and the amount of H₂ was determined by gas chromatography (GC-14C, Shimadzu, Japan, TCD, with nitrogen as a carrier gas and 5 \AA molecular sieve column).

3. Results and discussion

3.1. XRD analysis

X-ray diffraction measurement (XRD) was carried out to investigate the crystalline phase and the structure. Fig. 1 shows the XRD patterns of the ternary composite of TiO₂-CdS@g-C₃N₄, binary composites of TiO₂@g-C₃N₄ and CdS@g-C₃N₄, pristine CdS and g-C₃N₄. For g-C₃N₄ nanosheets, the distinct diffraction peak at 27.5° , corresponding to the inter-layer stacking of aromatic segments, can be indexed as the (002) diffraction plane for graphitic. After the

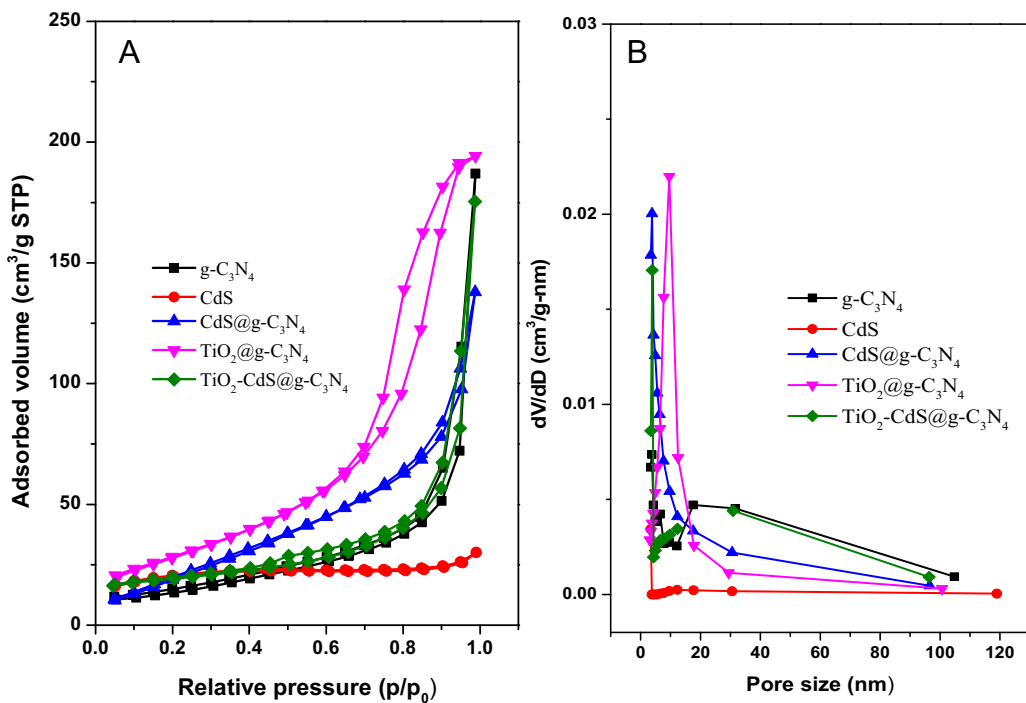


Fig. 3. N₂ adsorption-desorption isotherms (A) and pore size distribution curves (B) of the as-prepared g-C₃N₄, CdS, CdS@g-C₃N₄, TiO₂@g-C₃N₄ and TiO₂-CdS@g-C₃N₄.

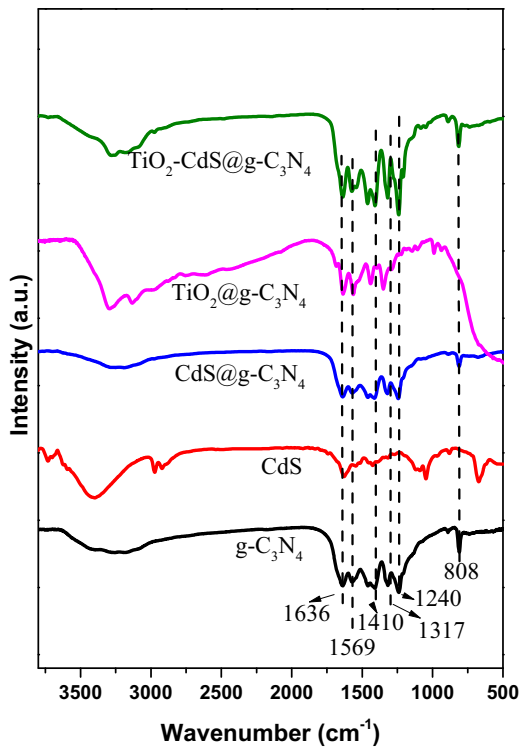


Fig. 4. FT-IR spectra of as-prepared g-C₃N₄, CdS, CdS@g-C₃N₄, TiO₂@g-C₃N₄ and TiO₂-CdS@g-C₃N₄.

modification of CdS or/and TiO₂ NDs onto the surface of g-C₃N₄, several typical peaks corresponding to CdS (JCPDS No. 80-10019) [31] and TiO₂ (JCPDS, No. 21-1272) [30] phases appear, indicating that CdS/TiO₂ NDs were successfully embellished on g-C₃N₄ during this mild hydrothermal process. The diffraction peaks in the composites of TiO₂@g-C₃N₄ and TiO₂-CdS@g-C₃N₄ are the typical peaks of anatase TiO₂.

Table 1

The specific surface areas, pore sizes and pore volumes data of the as-synthesized samples.

Catalyst	Surface area (m ² /g)	Pore size (nm)	Pore volume (cm ³ /g)
g-C ₃ N ₄	47.1	3.70	0.280
CdS	2.90	3.40	0.014
CdS@g-C ₃ N ₄	69.9	3.84	0.202
TiO ₂ @g-C ₃ N ₄	105.8	9.60	0.395
TiO ₂ -CdS@g-C ₃ N ₄	73.2	3.85	0.260

3.2. TEM, SEM and EDS analysis

To obtain the microstructure and microscopic morphology information of the ternary composite of TiO₂-CdS@g-C₃N₄ along with binary composites and pristine component, the transmission electron microscopy (TEM) test was carried out (Fig. 2 and Fig. S1). The smooth and flat layers of g-C₃N₄ can be clearly observed from Fig.S1-A, which is consistent with the previous reports. Pure CdS microspheres with an average diameter of 500 nm (Fig. 2A) have been obtained via the hydrothermal reaction. After the introduction of g-C₃N₄, CdS NDs can be densely and uniformly decorated onto its surface without aggregation (Fig. 2A). The size of CdS NDs prepared in the presence of lamellar g-C₃N₄ is decreased by two orders to that of pristine CdS microspheres obtained in the absence of g-C₃N₄. Likewise, as can be seen from Fig. 2C, TEM image of TiO₂-CdS@g-C₃N₄ ternary composite indicates that crystalline CdS and TiO₂ NDs are dispersed randomly with different orientations on the surface of the g-C₃N₄. Furthermore, no scattered particles can be observed from the outside of g-C₃N₄ nanosheets in the TEM images of Fig. 2B and C, suggesting the high level interaction between g-C₃N₄ nanosheets and TiO₂-CdS NDs. The HRTEM image (Fig. 2D) of TiO₂-CdS@g-C₃N₄ composite shows two different lattice fringes of 0.353 and 0.335 nm, belonging to (002) and (111) planes of anatase TiO₂ and CdS, according to the lattice parameters data in JCPDS, respectively. Fig. 2E shows the SEM image and EDS mapping of TiO₂-CdS@g-C₃N₄ sample. As exhibited in SEM image of Fig. 2E, the as-prepared ternary composite shows 3D loose structure, which

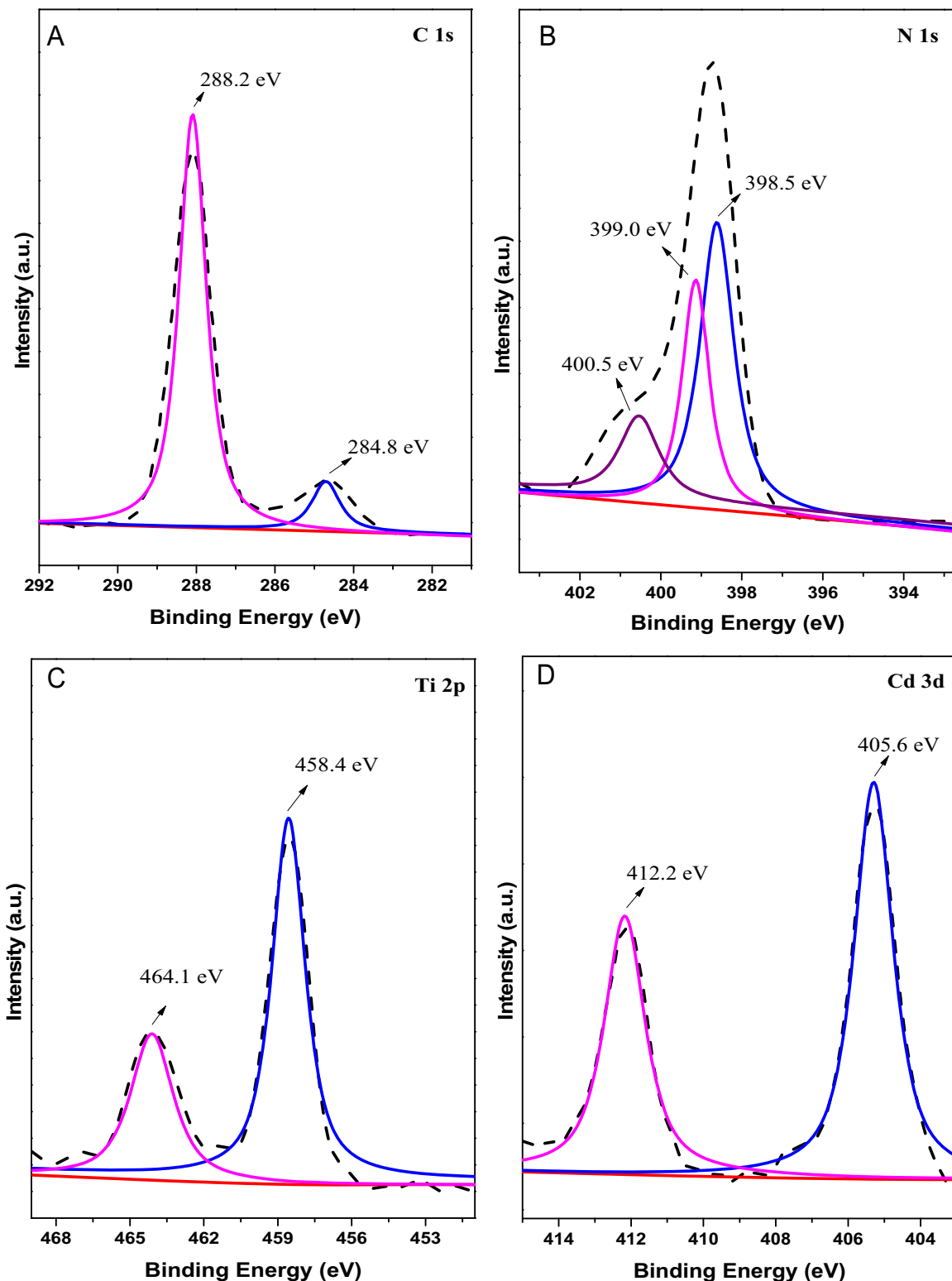


Fig. 5. XPS core-level spectra of C 1s, N 1s Ti 2p, and Cd 3d for the $\text{TiO}_2\text{-CdS@g-C}_3\text{N}_4$ composite.

may let more visible light inject into its inner and provide more reactive sites. The EDS mapping recorded from the area of the SEM image displays a homogeneous distribution of C, N, Cd, S and Ti elements. Moreover, the profiles of Ti, Cd and S are similar to that of C and N originated from $\text{g-C}_3\text{N}_4$ nanosheets, which indicates that the Ti, Cd and S elements are distributed uniformly and densely throughout the whole composite. Combining the XRD results and

the above analysis, it can be proved that the as-obtained sample should be ternary hybrid of $\text{TiO}_2\text{-CdS@g-C}_3\text{N}_4$.

3.3. N_2 adsorption-desorption analysis

The textural properties of as-prepared bare, binary and ternary samples were investigated using nitrogen gas porosime-

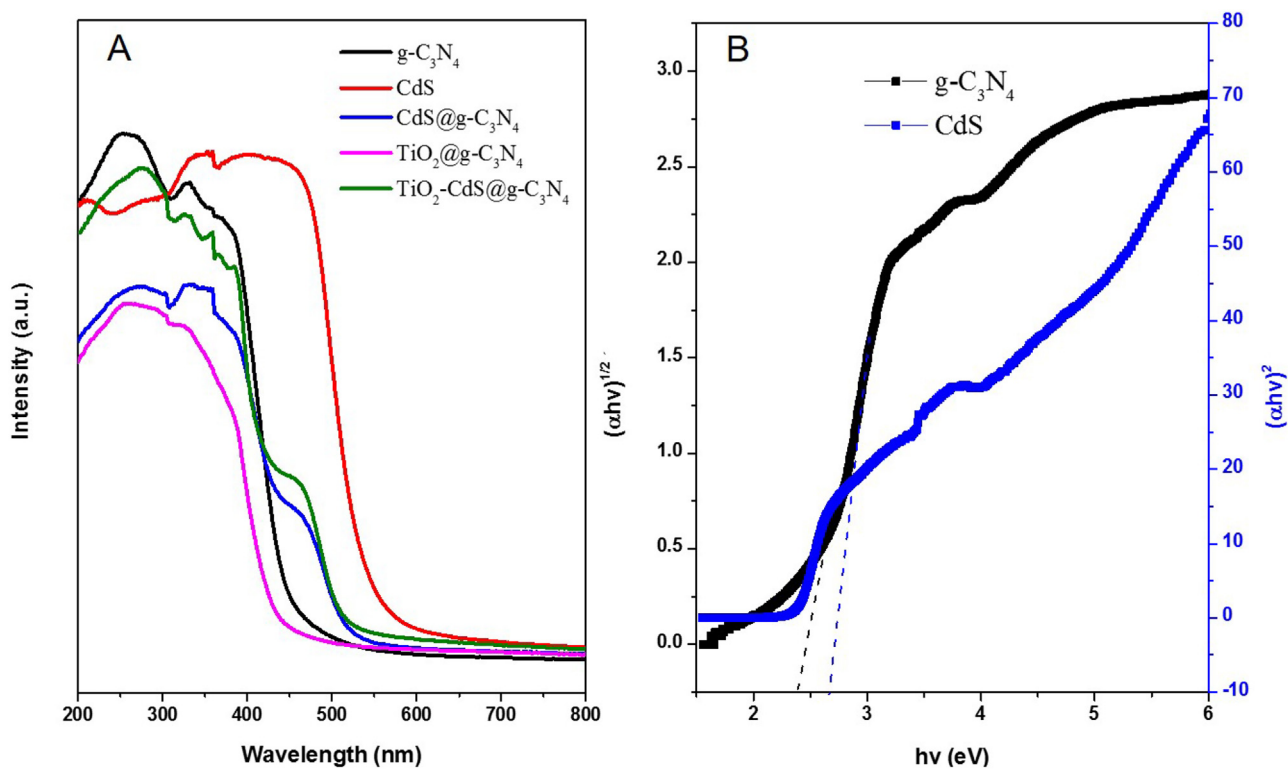


Fig. 6. UV-vis DRS spectra of as-prepared samples (A), Kubelka–Munk function transformed differential spectra of $\text{g-C}_3\text{N}_4$ and TiO_2 (B).

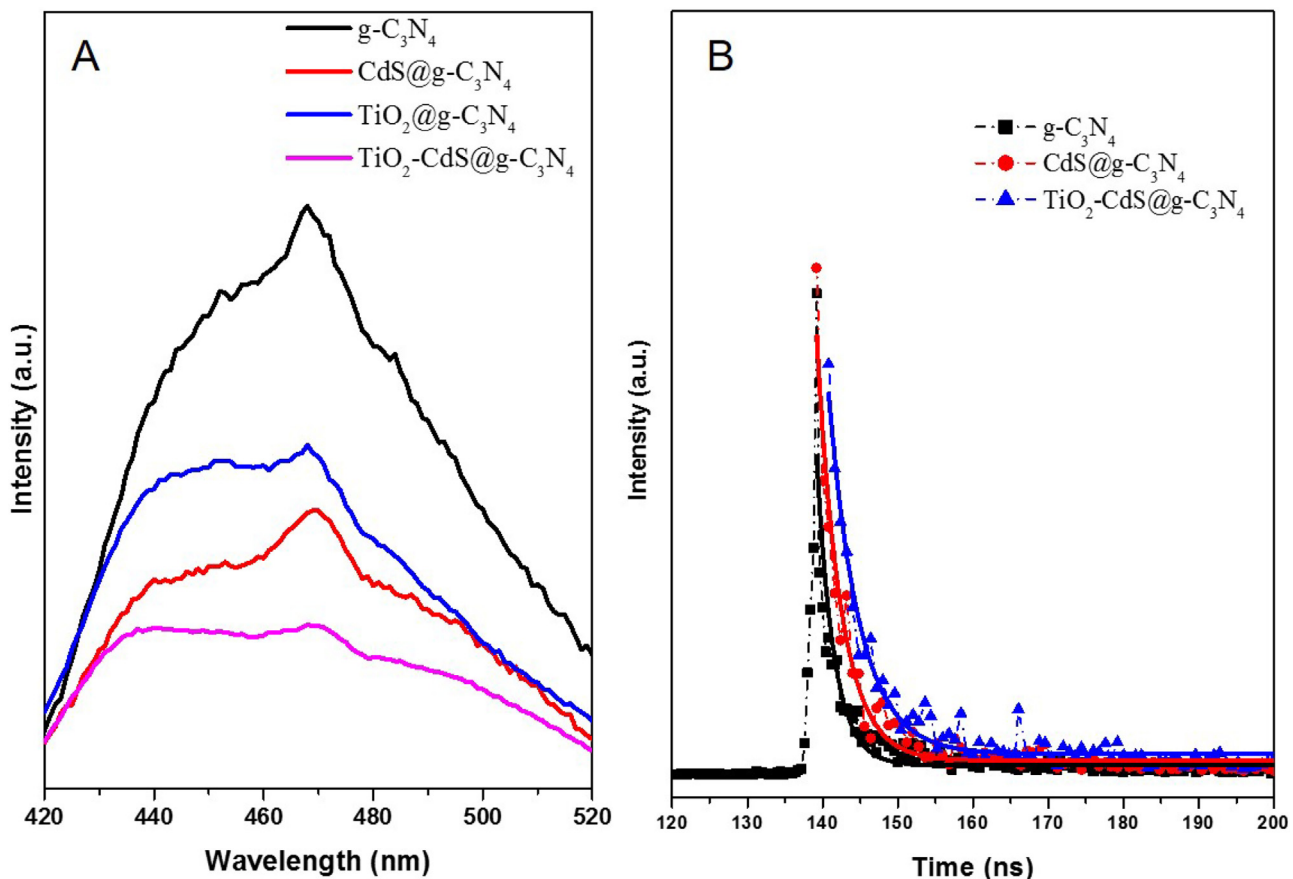


Fig. 7. PL spectra and time-resolved fluorescence decay spectra of as-synthesized photocatalysts.

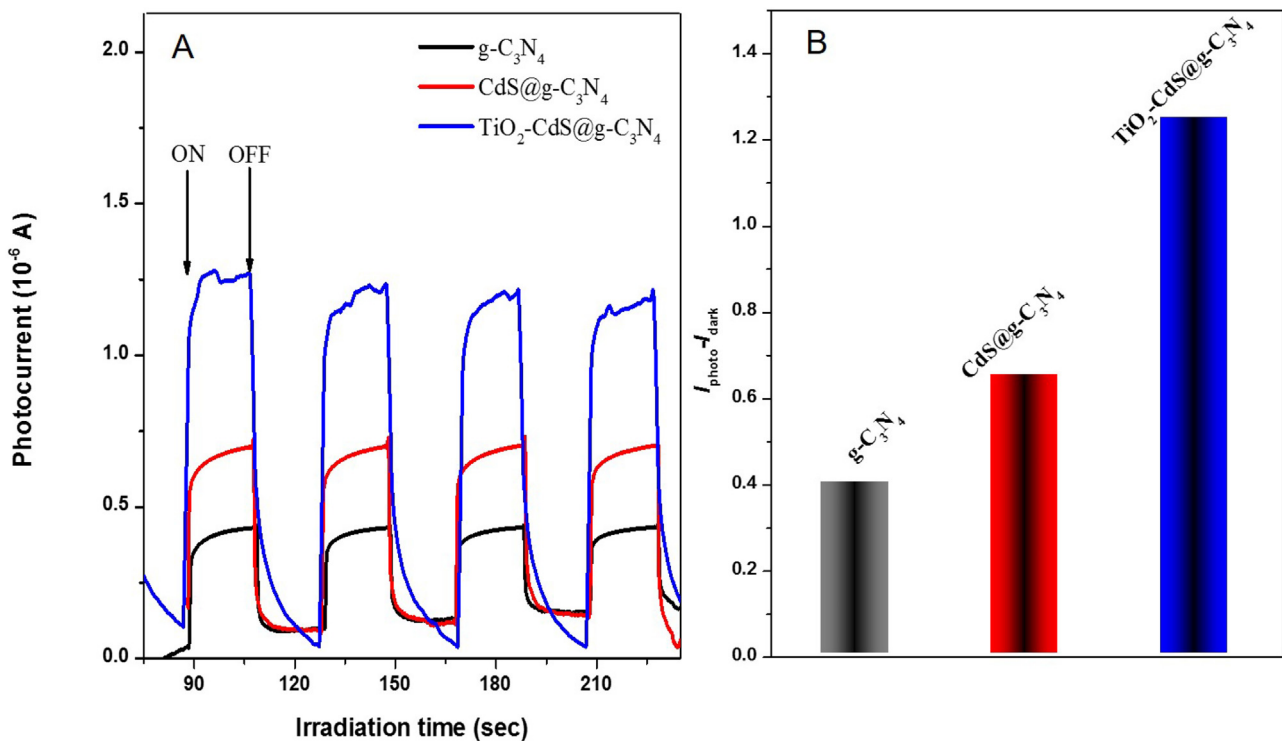


Fig. 8. Time-based photocurrent response (A) and photogenerated current ($I_{\text{photo}} - I_{\text{dark}}$) (B) of three typical as-prepared samples.

try measurement. Fig. 3 shows the nitrogen adsorption-desorption isotherms and pore size distribution curves of the five samples. Obviously, nitrogen adsorption-desorption isotherms of the g-C₃N₄ series samples are type IV with hysteresis loops according to the IUPAC classification [32], indicating the presence of mesopores within the composites. Bare CdS microspheres exhibit type IV isotherm, which do not contain micropores and mesopores. The Brunauer-Emmett-Teller (BET) specific surface areas, pore sizes and pore volumes of the as-synthesized photocatalysts calculated via BET and Barrett-Joyner-Halenda (BJH) methods are summarized in Table 1. The ternary TiO₂-CdS@g-C₃N₄ has a BET surface area of 73.2 m²/g, which is higher than those of pure g-C₃N₄ and CdS. The higher specific surface areas may be beneficial for the H₂ production because there being more reactive active sites for the adsorption water and other molecules, ease of transportation of them through the interconnected networks, and enhanced harvesting of light.

3.4. FT-IR analysis

FT-IR spectra were carried out to further determine the composition of TiO₂-CdS@g-C₃N₄ and other g-C₃N₄ based heterojunctions and the results were shown in Fig. 4. For pristine g-C₃N₄ nanosheets, the strong peaks at 1240, 1317, 1410, 1569 and 1636 cm⁻¹ can be attributed to the typical stretching vibration modes of C=N and C—N heterocycles [24]. The sharp peak at around 808 cm⁻¹ is assigned to the characteristic breathing mode of tri-s-triazine rings units [24]. For pure CdS, the broad peak at 660 cm⁻¹ and the band in 1050–1660 cm⁻¹ (except for 1630 cm⁻¹) region can be corresponded to the Cd-S bond [33]. In addition, the typical absorption peak of bare TiO₂ at 600 cm⁻¹ (not shown here) is ascribed to the Ti-O stretching mode, according to our previous report [34]. As for the binary (CdS@g-C₃N₄, TiO₂@g-C₃N₄) and ternary (TiO₂-CdS@g-C₃N₄) composites, the main characteristic breathing modes of TiO₂, CdS and g-C₃N₄ can be clearly observed, which indicated that TiO₂ and/or CdS NPs are successfully com-

bined with g-C₃N₄ nanosheets in the as-prepared composites. The broad peak that appears in the range of 2900–3600 cm⁻¹ is the stretching modes of the terminal NH₂ or groups at the defect sites of the aromatic ring [25].

3.5. XPS analysis

To determine the surface chemical compositions and the atomic valence states of the as-prepared crystals, X-ray photoelectron spectroscopy (XPS) was employed. Fig. 5A–D shows the high-resolution XPS spectra of C 1s, N 1s, Ti 2p and Cd 3d for the as-synthesized TiO₂-CdS@g-C₃N₄ ternary composite. As can be seen from Fig. 5A, the peak centered at 284.8 and 288.2 eV of C 1s can be assigned to carbon atoms in a purely carbonaceous environment (sp^2 C=C bonds, graphitic or amorphous carbons) and sp^2 -bonded carbon (N=C=N) in g-C₃N₄ network, respectively [34]. The N 1s (Fig. 5B) peak can be deconvoluted into three peaks at 398.5, 399.0 and 400.5 eV, which can be ascribed to N atoms sp^2 -bonded to two carbon atoms (C—N—C groups), tertiary nitrogen N-(C)₃ groups linking structural motif (C₆N₇) and amino functional groups having a hydrogen atom (C—N—H), respectively. In the Ti 2p spectrum, the peaks with binding energies of 458.4 eV and 464.1 eV are attributed to Ti 2p_{3/2} and Ti 2p_{1/2}, respectively, corresponding to Ti⁴⁺ oxidation state [36]. No peak assigned to Ti³⁺ species can be fitted. The photoelectron peaks of Cd 3d_{5/2} and Cd 3d_{3/2} levels located at 405.6 and 412.2 eV (Fig. 5D) can be attributed to the Cd²⁺ species of CdS in the composite of TiO₂-CdS@g-C₃N₄, which are very close to that reported before [37]. In combination, the XPS results present here further confirm the successful formation of TiO₂-CdS@g-C₃N₄ ternary photocatalyst. In addition, as compared with previous reports [35,36] about the binding energies of Ti 2p and Cd 3d in pure TiO₂ and CdS, those binding energies shift in the composite of TiO₂-CdS@g-C₃N₄. These could be attributed to the electronic effect/interaction among three components.

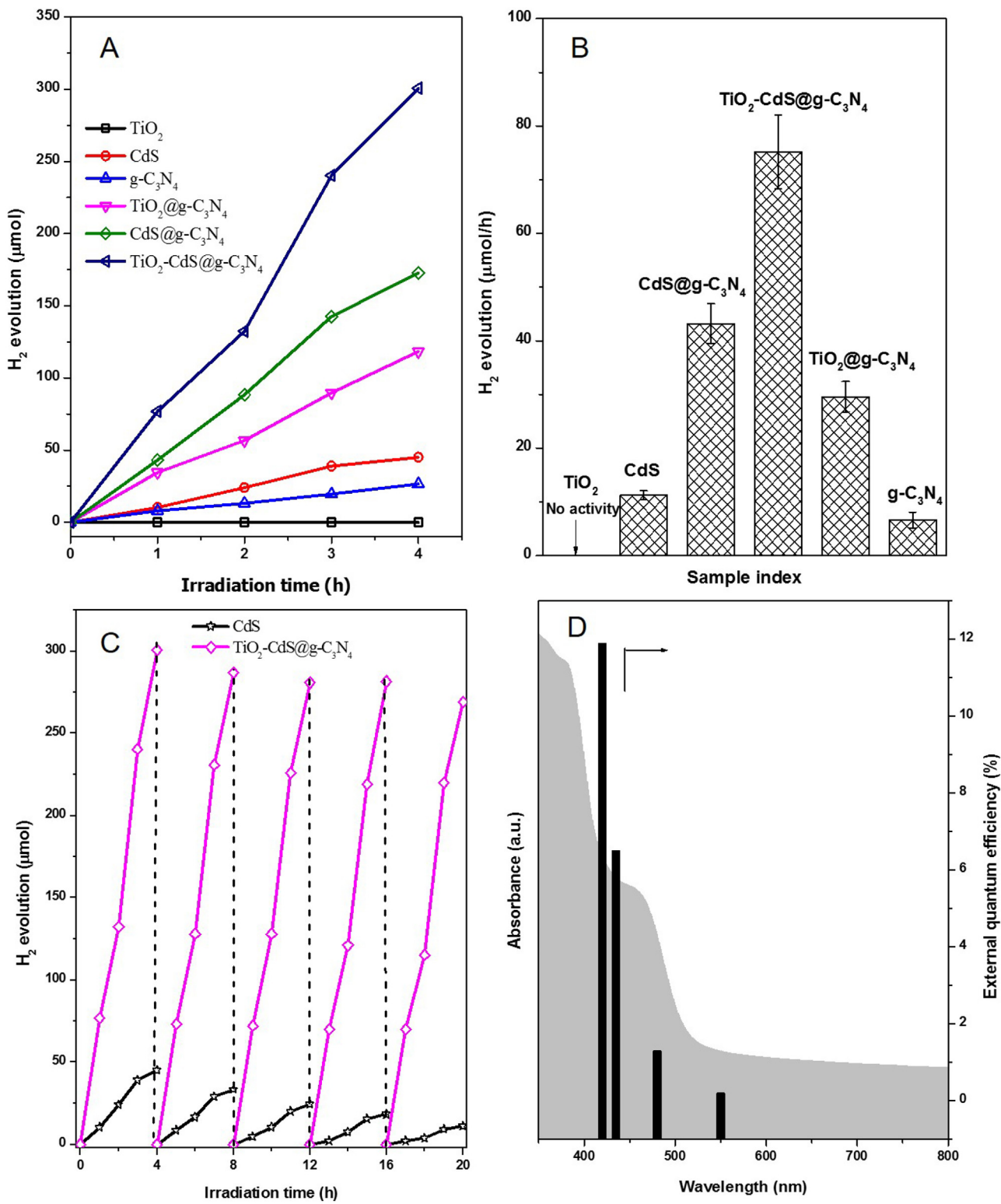


Fig. 9. Time courses of photocatalytic H₂ evolutions, average hydrogen production rates, the possibility of recycling ability of g-C₃N₄, CdS, CdS@g-C₃N₄, TiO₂@g-C₃N₄ and TiO₂-CdS@g-C₃N₄ under visible-light irradiation ($\lambda = 420$ nm) and EQE of TiO₂-CdS@g-C₃N₄.

3.6. UV-vis diffuse reflectance spectra analysis

The optical properties of as-prepared ternary and binary composites, as well as the pristine g-C₃N₄ and CdS were investigated using UV-vis diffuse reflectance spectroscopy (UV-vis DRS) and the results are shown in Fig. 6. For pure g-C₃N₄, it can absorb light with a

wavelength up to 450 nm, which is consistent with previous report [38]. As is known to all, anatase TiO₂ only absorbs ultraviolet light with a wavelength shorter than 400 nm (not shown here), matching the intrinsic inter-band transition absorption of pure anatase TiO₂. After combining with g-C₃N₄, binary composite of TiO₂@g-C₃N₄ shows visible light absorption range from 400 to 450 nm. For

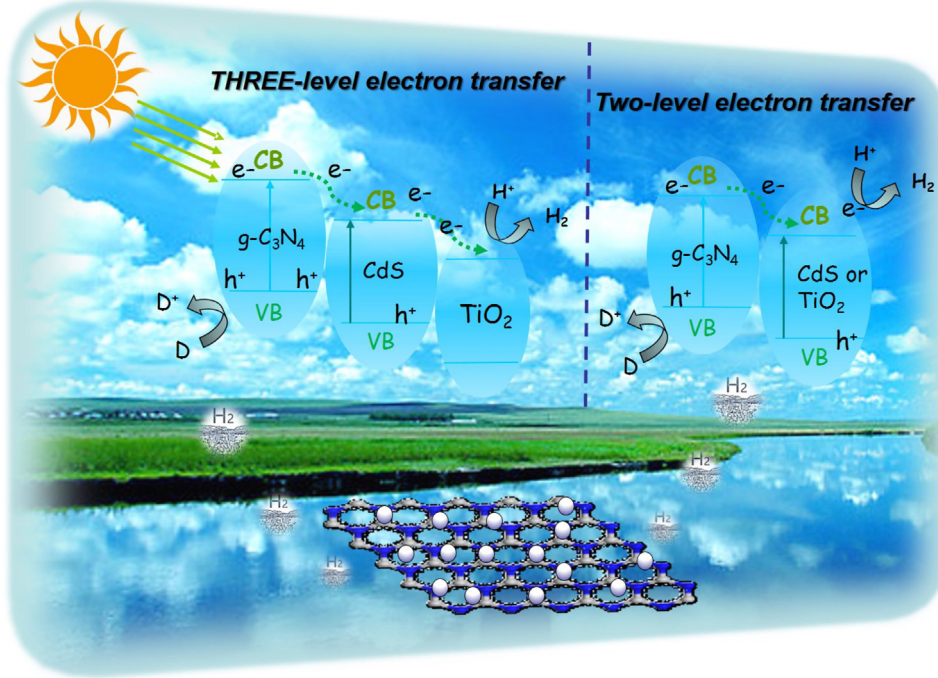


Fig. 10. Proposed mechanism for the enhanced visible-light photocatalytic H_2 evolution activity of the ternary composite.

pure CdS, the absorption edge close to 550 nm ($A_{\max} = 485$ nm) can be ascribed to the intrinsic band-gap transition of electron from the valence band (VB) to the conduction band (CB) of CdS [40]. From the UV-vis DRS spectra of CdS@g-C₃N₄ and TiO₂-CdS@g-C₃N₄, the maximum absorption peak is almost the same as the absorption of CdS, suggesting the existence of CdS in these composites. Furthermore, the addition of CdS NDs significantly enhanced the adsorption of the as-prepared materials in the visible-light region. Typically, the energy band-gap values of pure g-C₃N₄ and CdS were estimated using the Kubelka-Munk function:

$$\alpha h\nu = A(h\nu - E_g)^{n/2}$$

where α , h , ν , E_g , and A are the absorption coefficient, Planck constant, light frequency, band gap energy, and a constant, respectively. The coefficient n relies on the type of optical transition of a semiconductor ($n=1$ for direct transition and $n=4$ for indirect transition), being 1 for CdS [39] and 4 for g-C₃N₄ [38]. Based on this, the band-gap values of CdS and g-C₃N₄ are calculated to be 2.7 and 2.4 eV, respectively. (Fig. 6B).

3.7. Photoluminescence spectra analysis

It is well known that photoluminescence (PL) emission is important to disclose the fate of electron-hole pairs in semiconductor because PL emission is resulted from the recombination of photo-generated electrons and holes for some semiconductors. The higher intensity corresponds to the faster recombination. Fig. 7A shows the typical PL spectra of g-C₃N₄, CdS@g-C₃N₄, TiO₂@g-C₃N₄ and TiO₂-CdS@g-C₃N₄ excited in 360 nm. The main emission peak of g-C₃N₄ is centered at 468 nm, which can be contributed to the band-band PL phenomenon with the energy of light approximately equal to the band energy of g-C₃N₄ [39]. The results show that the modification of CdS/TiO₂ onto g-C₃N₄ drastically decreased the PL intensity of pristine g-C₃N₄. When both of CdS and TiO₂ NDs are decorated onto the surface of g-C₃N₄, the peak intensity further decreased for TiO₂-CdS@g-C₃N₄ comparing with the binary composites of CdS@g-C₃N₄ and TiO₂@g-C₃N₄. These results suggest that the heterostructure

among TiO₂, CdS and g-C₃N₄ can effectively diminish the electron-hole recombination rate. The PL intensity has strong effect on the photocatalytic activity of the corresponding photocatalysts. In order to better understand the behavior of the photogenerated electrons and holes, typical time-resolved fluorescence decay spectra of pristine g-C₃N₄, CdS@g-C₃N₄ and TiO₂-CdS@g-C₃N₄ were detected. The results indicate that the ternary composite of TiO₂-CdS@g-C₃N₄ exhibits the longest lifetime of carriers with respect to the binary CdS@g-C₃N₄ composite and single component of g-C₃N₄. The prolonged lifetime of photo-induced carriers on TiO₂-CdS@g-C₃N₄ is proposed to originate from long range three-electron transfer among three single components. A longer PL lifetime of carriers might be responsible for the improvement of photocatalytic activity.

3.8. Photoelectrochemical analysis

In order to further investigate the ability of generation, separation and migration efficiency of photogenerated carriers, photoelectrochemical measurements were performed. Fig. 8A shows the typical $I-t$ curves for as-prepared electrodes of g-C₃N₄, CdS@g-C₃N₄ and TiO₂-CdS@g-C₃N₄ with several on-off cycles of intermittent visible-light irradiation at a constant bias of 0.1 V vs. SCE with the measured solution pH of 7.4. Fig. 8B gives the photogenerated current ($I_{\text{photo}}-I_{\text{dark}}$) of g-C₃N₄, CdS@g-C₃N₄ and TiO₂-CdS@g-C₃N₄, where I_{photo} and I_{dark} represent the currents in the presence and absence of light irradiation, respectively. The photocurrent increases sharply when the light is switched on, and immediately returns to its initial state after the light source is turned off, which is repeatable [41,42]. This result indicates that the as-prepared samples show excellent structural stabilities. The transient photocurrent density of CdS@g-C₃N₄ is 1.25 times higher than that of pure g-C₃N₄. The higher photocurrent density demonstrates more efficient charge separation and transportation. It is also found that the transient photocurrent response of TiO₂-CdS@g-C₃N₄ ternary composite is the highest among the as-tested three

samples own to the junction-promoted efficient three-level electron charge separation and improved light absorption.

3.9. Hydrogen generation activity

To evaluate the photocatalytic performance of the as-prepared photocatalysts, hydrogen evolution experiments from water splitting were carried out under visible light irradiation in the presence of Na_2S (0.5 M) and Na_2SO_3 (0.5 M) solution. Fig. 9A shows curves of H_2 evolution kinetic lines, indicating that the amount of H_2 increases with the time irradiated by the visible light (420 nm). It can be seen that the ternary composite of $\text{TiO}_2\text{-CdS@g-C}_3\text{N}_4$ and binary hybrid materials of $\text{TiO}_2@\text{g-C}_3\text{N}_4$ and $\text{CdS@g-C}_3\text{N}_4$ show improved photocatalytic hydrogen generation activity as compared to their single components of TiO_2 , CdS and $\text{g-C}_3\text{N}_4$. In addition, the $\text{TiO}_2\text{-CdS@g-C}_3\text{N}_4$ exhibits the highest hydrogen production activity. Fig. 9B gives average hydrogen production rates of as-obtained samples. No noticeable H_2 was produced for pure TiO_2 . The hydrogen production rate on pristine $\text{g-C}_3\text{N}_4$ is very low and is only 6.7 $\mu\text{mol}/\text{h}$. Pure CdS generates 11.3 μmol hydrogen every hour. The hydrogen evolution rate of $\text{TiO}_2@\text{g-C}_3\text{N}_4$ and $\text{CdS@g-C}_3\text{N}_4$ reaches 43.2 and 29.6 $\mu\text{mol}/\text{h}$, respectively. These production rates are 6.4 and 4.4 times higher than that of pure $\text{g-C}_3\text{N}_4$. $\text{TiO}_2\text{-CdS@g-C}_3\text{N}_4$ hybrid material shows the most efficient H_2 evolution rate (75.2 $\mu\text{mol}/\text{h}$), which is 11.2 times higher than that of $\text{g-C}_3\text{N}_4$. Moreover, this value is also higher than those of binary composites ($\text{TiO}_2@\text{g-C}_3\text{N}_4$ and $\text{CdS@g-C}_3\text{N}_4$) under the same irradiation wavelength (420 nm) and most works of reported photocatalysts (Supporting information, Table S1). These results suggest that the hydrogen production rates of TiO_2 and CdS NDs are significantly enhanced by coupling with the $\text{g-C}_3\text{N}_4$ nanosheets. This is resulted by the heterojunction electric field among the TiO_2 , CdS and $\text{g-C}_3\text{N}_4$. Stability and reusability are pivotal for photocatalysts in practical applications. In order to obtain the stability information of as-prepared photocatalysts, the recycling photocatalytic test of hydrogen evolution on CdS and $\text{TiO}_2\text{-CdS@g-C}_3\text{N}_4$ was carried out for five times under the same experimental condition. Fig. 9C exhibits the photocatalytic stability measurement of the two samples. During the consecutive 5 runs over 20 h, no noticeable decrease can be detected in hydrogen production rate for $\text{TiO}_2\text{-CdS@g-C}_3\text{N}_4$, which suggesting that the photocatalyst keeps good photo-stabilization throughout the testing cycles. Fig. S2 shows the XRD patterns of $\text{TiO}_2\text{-CdS@g-C}_3\text{N}_4$ which have been used for 5 recycling runs. The result shows that the phase and structure remain intact, indicating that the ternary photocatalyst is stable in the hydrogen generation process. The result also reveals that the hydrogen generation activity of CdS is obviously declined after five cycles due to the well-known photocorrosion induced by the photo-induced holes. Furthermore, to investigate the solar energy conversion efficiency, external quantum efficiency (EQE) with different single wavelengths was tested. The ternary composite of $\text{TiO}_2\text{-CdS@g-C}_3\text{N}_4$ has a QE of 11.9% at 420 nm (Fig. 9D), which is higher than most of the reported catalysts (Supporting information, Table S1), implying the high utilization efficiency of photo-induced charges. The QE of $\text{TiO}_2\text{-CdS@g-C}_3\text{N}_4$ is tested to be 6.5, 1.3 and 0.2 at the wavelength of 435, 480 and 550, respectively, indicating that the as-obtained composites still exhibit good solar energy conversion efficiency towards the hydrogen evolution under $\lambda > 420$ nm visible light irradiation.

3.10. Possible mechanism

Based on the above experimental results, it can be concluded that the enhanced visible-light photocatalytic hydrogen evolution

activity of $\text{TiO}_2\text{-CdS@g-C}_3\text{N}_4$ is attributed to the following factors (Fig. 10).

- (1) Obviously, the BET surface area of $\text{TiO}_2\text{-CdS@g-C}_3\text{N}_4$ is similar with $\text{CdS@g-C}_3\text{N}_4$ and smaller than $\text{TiO}_2@\text{g-C}_3\text{N}_4$ to some degree. Ternary composite of $\text{TiO}_2\text{-CdS@g-C}_3\text{N}_4$ photocatalyst exhibits a profound improvement in H_2 evolution activity, as compared to binary materials of $\text{TiO}_2@\text{g-C}_3\text{N}_4$ and $\text{CdS@g-C}_3\text{N}_4$. The enhanced photocatalytic activity can be attributed to the long-distance electron transport of the three-level electron transfer system rather than the differences in BET surface area and porosity of the catalysts.
- (2) As a polymeric semiconductor with visible-light absorption, $\text{g-C}_3\text{N}_4$ can not only effectively improve the visible light absorption but also disperse NDs onto itself to limit the aggregation. As evidenced in N_2 adsorption-desorption section, the BET surface areas of as-prepared composites are higher than their components, which can be used to provide more adsorption sites and active sites (this can be ascribed to the large contact area provided by the unique 0D-2D structure). Meanwhile, as can be observed from TEM analysis, TiO_2 and CdS NDs are dispersed on the surface of $\text{g-C}_3\text{N}_4$ without aggregation. Furthermore, the 2D structure of $\text{g-C}_3\text{N}_4$ nanosheets can facilitate the effective transportation of products and photo-induced carriers.
- (3) The improved H_2 evolution activity of $\text{TiO}_2\text{-CdS@g-C}_3\text{N}_4$ also attributed to matched energy level position among TiO_2 , CdS and $\text{g-C}_3\text{N}_4$ and visible light harvesters of CdS NDs (narrow bandgap). As discussed in UV-vis DRS section and the previous report, the CB and VB positions of the TiO_2 (CdS) are ~ -0.29 eV (-0.52 eV) and $+2.91$ eV ($+1.88$ eV), while those of the $\text{g-C}_3\text{N}_4$ are ~ -1.13 and $+1.57$ V, respectively. When the visible light is irradiated on the surface of the catalysts, the photo-generated electrons in the CB of CdS and $\text{g-C}_3\text{N}_4$ tends to transfer to the CB of TiO_2 , meanwhile the holes in the VB of CdS will move to the VB of $\text{g-C}_3\text{N}_4$. With this process, the photo-induced carriers within this ternary system can be successfully separated, thus excellent photocatalytic activity can be achieved.

In a brief word, the improved H_2 evolution activity of as-fabricated ternary material of $\text{TiO}_2\text{-CdS@g-C}_3\text{N}_4$ can be ascribed to the good charge separation of three-level electron transfer system, matched energy levels of TiO_2 , CdS and $\text{g-C}_3\text{N}_4$, good visible-light adsorption ability, robust 0D-2D geometry construction, the abundant adsorption sites and active sites.

4. Conclusion

In summary, a novel three-level electron transfer system of $\text{TiO}_2\text{-CdS@g-C}_3\text{N}_4$ has been successfully obtained by decorating $\text{TiO}_2\text{-CdS}$ NDs onto the surface of $\text{g-C}_3\text{N}_4$ nanosheets. $\text{TiO}_2\text{-CdS@g-C}_3\text{N}_4$ hybrid material shows the most efficient H_2 evolution rate (75.2 $\mu\text{mol}/\text{h}$), which is 11.2 times higher than that of $\text{g-C}_3\text{N}_4$. The QE value reaches up to 11.9% at 420 nm. Compared with the binary composites and their single components, the formed 0D-2D, three-level electron transfer system originated from the suitable band level structure of $\text{TiO}_2\text{-CdS@g-C}_3\text{N}_4$ can not only provide more adsorption sites and active sites to produce synergistic effect but also accelerate the separation of photo-induced electrons and holes. Moreover, compared to pure CdS , the ternary composite exhibits comparable H_2 evolution activity after 5 runs over 20 h, revealing its good photo-stability and applicability in the long-term water splitting. This work can provide a facile yet efficient way to design 0D-2D, three-level electron transfer system for hydrogen production.

Acknowledgements

The authors gratefully acknowledged the National Natural Science Foundation (21607063, 21676129), Hong Kong Scholar Program (XJ2016034), China.

Appendix A. Supplementary data

Supplementary data associated with this article can be found, in the online version, at <http://dx.doi.org/10.1016/j.apcatb.2017.03.069>.

References

- [1] A. Kubacka, M. Fernández-García, G. Colón, Chem. Rev. 112 (2012) 1555.
- [2] S. Guo, T. Zhao, J. Quan, S. Han, J. Power Sources 293 (2015) 17.
- [3] M. Pelaeza, N. Nolanb, S. Pillaib, M. Seeryc, P. Falarasd, A. Kontosd, P. Dunlope, J. Hamiltone, J. Byrnee, K. O'Sheaf, M. Entezarig, D. Dionysioua, Appl. Catal. B: Environ. 125 (2012) 331.
- [4] X. Zhang, G. Zuo, X. Lu, C. Tang, S. Cao, M. Yu, J. Colloid Interface Sci. 490 (2017) 774.
- [5] J. Yu, J. Low, W. Xiao, P. Zhou, M. Jaroniec, J. Am. Chem. Soc. 136 (2014) 8839.
- [6] X. Yu, J. Yu, B. Cheng, M. Jaroniec, J. Phys. Chem. C 113 (2009) 17527.
- [7] H. Yu, P. Xiao, J. Tian, F. Wang, J. Yu, ACS Appl. Mater. Interfaces 8 (2016) 29470.
- [8] G. Li, D. Zhang, J.C. Yu, Environ. Sci. Technol. 43 (2009) 7079.
- [9] C. Li, F. Wang, J. Zhu, J.C. Yu, Appl. Catal. B: Environ. 100 (2010) 433.
- [10] X. An, X. Yu, J.C. Yu, G. Zhang, J. Mater. Chem. A 1 (2013) 5158.
- [11] Z. Hu, J.C. Yu, J. Mater. Chem. A 1 (2013) 12221.
- [12] G. Li, L. Wu, F. Li, P. Xu, D. Zhang, H. Li, Nanoscale 5 (2013) 2118.
- [13] X. Li, J. Zhu, H. Li, Appl. Catal. B: Environ. 123–124 (2012) 174.
- [14] H. Cheng, X. Lv, S. Cao, Z. Zhao, Y. Chen, W. Fu, Sci. Rep. 6 (2016) 19846.
- [15] X. Yin, L. Li, W. Jiang, Y. Zhang, X. Zhang, L. Wan, J. Hu, ACS Appl. Mater. Interfaces 8 (2016) 15258.
- [16] M. Zeng, Z. Chai, X. Deng, Q. Li, S. Feng, J. Wang, D. Xu, Nano Res. 9 (2016) 2729.
- [17] Y. Xu, Y. Ye, T. Liu, X. Wang, B. Zhang, M. Wang, H. Han, C. Li, J. Am. Chem. Soc. 138 (2016) 10726.
- [18] M. Jana, U. Gupta, C.N.R. Rao, Dalton Trans. 45 (2016) 15137.
- [19] X. Li, J. Wang, Y. Men, Z. Bian, Appl. Catal. B: Environ. 187 (2016) 115.
- [20] Y. Huo, X. Yang, J. Zhu, H. Li, Appl. Catal. B: Environ. 106 (2011) 69.
- [21] Z. Meng, M. Peng, L. Zhu, W. Oh, F. Zhang, Appl. Catal. B: Environ. 113–114 (2012) 141.
- [22] X. Chen, S. Shen, L. Guo, S. Mao, Chem. Rev. 110 (2010) 6503.
- [23] (a) L. Lin, H. Ou, Y. Zhang, X. Wang, ACS Catal. 6 (2016) 3921;
(b) X. Wang, K. Maeda, A. Thomas, K. Takanabe, G. Xin, J.M. Carlsson, K. Domen, M. Antonietti, Nat. Mater. 8 (2009) 76.
- [24] D. Zheng, X. Cao, X. Wang, Angew. Chem. Int. Ed. 55 (2016) 11512.
- [25] J. Zhang, M. Zhang, L. Lin, X. Wang, Angew. Chem. Int. Ed. 54 (2015) 6297.
- [26] X. Wang, W. Yang, F. Li, Y. Xue, R. Liu, Y. Hao, Ind. Eng. Chem. Res. 52 (2013) 17140.
- [27] K. Li, S. Gao, Q. Wang, H. Xu, Z. Wang, B. Huang, Ying Dai, J. Lu, ACS Appl. Mater. Interfaces 7 (2015) 9023.
- [28] J. Zhang, Y. Wang, J. Jin, J. Zhang, Z. Lin, F. Huang, J. Yu, ACS Appl. Mater. Interfaces 5 (2013) 10317.
- [29] Z. Jiang, C. Zhu, W. Wan, K. Qian, J. Xie, J. Mater. Chem. A 4 (2016) 1806.
- [30] Z. Jiang, D. Jiang, Z. Yan, D. Liu, K. Qian, J. Xie, Appl. Catal. B: Environ. 170 (2015) 195.
- [31] W. Li, C. Feng, S. Dai, J. Yue, F. Hua, H. Hou, Appl. Catal. B: Environ. 168–169 (2015) 465.
- [32] J. Liu, M. Zheng, X. Shi, H. Zeng, H. Xia, Adv. Funct. Mater. 26 (2016) 919.
- [33] L. Ge, F. Zuo, J. Liu, Q. Ma, C. Wang, D. Sun, L. Bartels, P. Feng, J. Phys. Chem. C 116 (2012) 13708.
- [34] Z. Jiang, J. Xie, RSC Adv. 6 (2016) 3186.
- [35] S. Zhou, Y. Feng, L. Zhang, Mater. Lett. 57 (2003) 2936.
- [36] Z. Jiang, W. Wan, W. Wei, K. Chen, H. Li, P.K. Wong, J. Xie, Appl. Catal. B: Environ. 204 (2017) 283.
- [37] Z. Chen, S. Liu, M. Yang, Y. Xu, ACS Appl. Mater. Interfaces 5 (2013) 4309.
- [38] C. Li, Y. Du, D. Wang, S. Yin, W. Tu, Z. Chen, M. Kraft, G. Chen, R. Xu, Adv. Funct. Mater. 2017 (1604) 328.
- [39] K. Li, M. Han, R. Chen, S. Li, S. Xie, C. Mao, X. Bu, X. Cao, L. Dong, P. Feng, Y. Lan, Adv. Mater. 28 (2016) 8906.
- [40] T. Simon, M.T. Carlson, J.K. Stolarczyk, J. Feldmann, ACS Energy Lett. 1 (2016) 1137.
- [41] Y.Y. Bu, Z.Y. Chen, W.B. Li, Appl. Catal. B 144 (2014) 622.
- [42] Y.J. Zhang, T. Mori, L. Niu, J.H. Ye, Energy Environ. Sci. 4 (2011) 4517.